Dalton Transactions

ROYAL SOCIETY OF CHEMISTRY

PERSPECTIVE

View Article Online
View Journal | View Issue

Cite this: *Dalton Trans.*, 2022, **51**, 16428

Recent advances in luminescent metallacycles/metallacages for biomedical imaging and cancer therapy

Yida Pang,†[a,b] Chonglu Li,†[b] Hongping Deng*[a] and Yao Sun *[b]

Received 25th August 2022,
Accepted 23rd September 2022

DOI: 10.1039/d2dt02766f

rsc.li/dalton

Small molecule metal-based drugs have shown great achievements in preclinical and clinical applications. In particular, platinum based antitumor drugs are well established in current cancer chemotherapy. However, they face problems such as poor selectivity, severe toxicity and side effects, strong drug resistance, poor uptake/retention *in vivo*, and difficulty in monitoring the therapeutic effect in real time, which largely limit their widespread use in clinical applications. The metallacycles/metallacages formed by the coordination-driven self-assembly of highly emitting ligands can solve the above problems. Importantly, acceptors with chemotherapeutic properties in the metallacycles/metallacages can be combined with luminescent ligands to achieve a combination of chemotherapy, imaging contrast agents and multifunctional therapeutic platforms. Here, this review provides an insight into the paradigm of self-assembled metallacycles/metallacages in biological applications, from mono-chemotherapeutic drugs to excellent fluorescent imaging contrast agents and multifunctional therapeutic platforms.

1. Introduction

According to the statistics of the International Agency for Research on Cancer, in 2020, there were about 19.3 million new cancer cases and about 10 million malignant tumor deaths in the world.[1] Chemotherapy is one of the main options for cancer patients and is widely used in clinical trials. It has achieved great success in inhibiting tumor growth, reducing tumor recurrence, and inhibiting cancer metastasis.[2]

Platinum-based chemotherapeutics are the solely viable metal-based chemotherapeutics currently used in clinics for tumor ablation and can be used as templates for the development of new metal-based anticancer drugs.[3] Actually, all commercially available platinum-based metal drugs employ the mechanism of cisplatin, which forms covalent bonds with DNA, with the aim of resisting the DNA repair system to activate tumor cell death mechanisms.[4] However, these drugs also suffer from serious adverse reactions and high drug resistance, such as nephrotoxicity, peripheral neurotoxicity, myelopathy and intense alopecia.[5] Scientists have explored a variety of approaches to address these issues; for example, ruthenium complexes with anticancer activity were preferred, as they have variable oxidation states, similar ligand exchange kinetics to Pt and similar biomolecule binding modes to Fe in physiological environments, which endow them with high antitumor activity, the ability to reduce metastasis, and generally low systemic toxicity.[6] In addition, the synthesis of metal prodrugs,[7] the preparation of targeted drug molecules,[8] and the search for more appropriate metal receptors[9] have been of great benefit in addressing these issues. Nonetheless, these small molecule drugs still face poor uptake/retention in organisms and monitoring their therapeutic effect in real time is difficult, which greatly compromise the therapeutic efficiency of chemotherapeutic drugs. Fortunately, coordinated self-assembly strategies based on organic ligands and metal receptors may be able to address these challenges.

Based on coordination driven self-assembly between Lewis basic organic donors and Lewis acidic metal acceptors, discrete supramolecular coordination complexes (SCCs) with various sizes and shapes have been well constructed.[10] Compared to the corresponding small-molecule precursors, the large metallacycle/metallacage structure of SCCs enhanced their cellular uptake and retention and allowed for high affinity binding to biomolecules. Besides, they even enabled access to new functions that were not available with individual molecular components.[11] In addition, with the introduction of ligands with good luminescence properties, the metallacycles/metallacages can lead to spatio-temporally controllable metal chemotherapeutic drugs for diagnosis and treatment

[a]*Department of Vascular Surgery, Remin Hospital of Wuhan University, Wuhan 430079, P. R. China. E-mail: hpdeng@whu.edu.cn*
[b]*Key Laboratory of Pesticide and Chemical Biology, Ministry of Education, College of Chemistry, Central China Normal University, Wuhan 430079, P. R. China. E-mail: sunyaogbasp@ccnu.edu.cn*
†These authors contributed equally to this work.

integration. The self-assembly between ligands and acceptors will also greatly improve the photophysical properties of ligands, such as the inhibition of π–π stacking of organic ligands and the bathochromic shift of the wavelength of ligands, which effectively improved the fluorescence imaging performance of metallacycles/metallacages.[12] More importantly, some luminescent ligands can initiate photodynamic therapy and photothermal therapy under irradiation with specific light, which is a kind of treatment modality not limited by radiation or chemotherapy resistance and can be a potential therapeutic modality for localized cancers, such as oropharyngeal cancer, cervical cancer and esophageal cancer.[13]

However, due to the resistance of intratumoral hypoxia to photodynamic therapy and the overexpression of heat shock proteins in cancer cells during photodynamic therapy, the efficiency of phototherapy is low.[14] Fortunately, the advantages such as metal ion-promoted conversion of the ligand singlet to triplet state, the appropriate ligand-to-metal energy transfer, and the inhibition of intramolecular motion of the organic backbone in the rigid framework can be used to solve the problems in phototherapy.[15] The platform of integrating accurate imaging, phototherapy and chemotherapy with metallacycles/metallacages provided researchers with novel ideas in cancer diagnosis and treatment. Here, this review provides an insight into the paradigm of self-assembled metallacycles/metallacages in biological applications, from mono-chemotherapeutic drugs to excellent fluorescent imaging contrast agents and multifunctional therapeutic platforms.

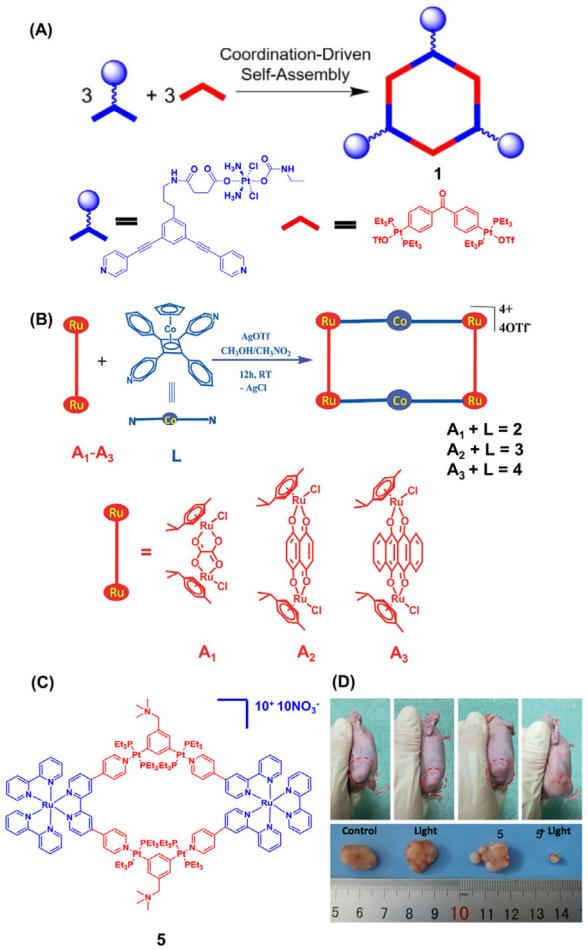

Fig. 1 (A) Structure of metallacycle **1**; (B) structures of metallacycles **2–4**; (C) structure of metallacycle **5**; (D) the tumor inhibition of **5** + light and control groups; the figure adapted from ref. 18 with permission from the National Academy of Sciences, Copyright 2018.

2. Application of metallacycles/metallacages in tumor imaging and treatment

In the classical metal drug-based therapy, anticancer drugs directly targeted DNA according to the cisplatin pattern, forming intra- and inter-strand crosslinks and finally triggering cell death. Efforts have been made to design highly targeted drug delivery systems to counteract the high systemic toxicity of metal-based anticancer drugs. In 2018, Yang *et al.* reported that the Pt(IV) precursor drug macrocycle **1** (Fig. 1A) had an extremely low half-inhibitory concentration (IC_{50} = 0.87 ± 0.13 μM) on A549 cells and showed that compound **1** could easily enter cancer cells and release cisplatin to damage DNA and trigger apoptosis for cancer cell inhibition.[16] Chi *et al.* carried out a more in-depth study, and they reported that the cobalt–ruthenium heterometallic rectangular molecules **2–4** (Fig. 1B), which were formed from a new ditopic cobalt sandwich ligand and a class of *p*-cymene ruthenium(II) acceptors effectively achieved the anticancer effect by inducing apoptosis and autophagy of human cancer cells.[17] In 2018, Stang's group used a $[Ru(II)(2,2'\text{-bipyridine})_3]^{2+}$ derivative and Pt-based quaternary ammonium salt and rationally constructed a new two-photon treatment mode Pt–Ru photosensitizer **5** (Fig. 1C), which can effectively generate $^1O_2$ under light excitation. Its highly charged nature endowed the macrocycle **5** with the ability to accelerate its internalization, selectively accumulate in the mitochondria and nucleus[18] and finally effectively trigger cancer cell death. This approach can achieve a higher tumor inhibition rate in combination with chemotherapy (Fig. 1D).

However, due to the fuzzy boundary and easy metastasis of malignant tumors, although the prepared metal–organic macrocycles have excellent anti-cancer effects in *in vitro* experiments, the introduction of ligands with better imaging capability is required to effectively facilitate the precise localization in tumors for successful tumor resection. In general, traditional organic fluorophores with a better fluorescence quantum yield can be introduced into the metal–organic macrocyclic framework for a better imaging effect.

The traditional aggregation-induced emission molecule tetraphenylethylene (TPE) has excellent imaging properties in the aggregated state, but it is difficult for metal complexes with only TPE in the structure to change the wavelength too

much. Both difluoroboron dipyrromethenes (BODIPY) and porphyrin have the advantages of large conjugated planes, high quantum yield, *etc*., and are photodynamic and photothermal therapy candidates, but severe π–π stacking and low water solubility limit their use in biological applications. With regard to these organic light-emitting ligands, in general, after delicate modification by researchers, unexpected results may be achieved. Here, we mainly discuss fluorescent imaging metal–organic macrocycles/cages with TPE, porphyrin and BODIPY as ligands.

2.1. TPE-based metallacycles/metallacages for cancer imaging and therapy

TPE was first synthesized by Boissieu and coworkers in 1888, and it was an excellent aggregation-induced emission agent (AIEgen).[19,20] The fluorescence signal of AIE probes is only generated when their intermolecular rotation is restricted or aggregates are formed; thus they have excellent resistance to photobleaching, as well as superior photostability and high signal reliability.[21] In addition, AIEgen luminescent probes have a high signal-to-noise ratio, which make them particularly attractive for continuous visualization of biological processes that do not require repeated cleaning.[22] Yang's group synthesized the discrete TPE–metal platinum macrocycle **6** (Fig. 2A) for bioimaging. Amphiphilic species (NIPAAM) were modified on the metal macrocyclic skeleton,[23] and the obtained super amphiphilic metal–organic species can self-assemble into fluorescent nanoparticles in water. Furthermore, the good AIE properties and biocompatibility of this metal macrocycle allowed its excellent imaging performance in cancer cells (Fig. 2B).

The combination of diagnostic ability and treatment activity in a treatment platform aims at improving the efficiency of cancer treatment. Stang *et al.* constructed a metallacage **7** (Fig. 2C), which integrated imaging and treatment by unifying self-assembly, coordination chemistry and supramolecular chemistry.[24] By incorporating TPE into the components of the self-assembled quadrilateral metal frame, nanoparticles (7-NPs) with a diameter of 35 nm were prepared through encapsulation with a mixture of mPEG–DSPE and biotin–PEG–DSPE. The EPR effect and active targeting enabled the 7-NPs to accumulate in HeLa cells and HepG2 cellswith excellent cell imaging ability. The intense fluorescence of 7-NPs enabled imaging techniques to monitor the pharmacokinetics of HeLa tumor mice. The 7-NPs efficiently accumulated at the tumor site with their signal persisting even for 24 hours after a single injection (Fig. 2D). Compared with free platinum anticancer drugs (oxaliplatin, carboplatin and cisplatin), 7-NPs had higher antitumor efficacy (Fig. 2E) and lower systemic toxicity.

Compared with the macrocycle containing only TPE fluorophores in the skeleton, the introduction of long wavelength organic ligands in the macrocycle skeleton is more propitious to perform imaging *in vivo*. Mao *et al.* developed a therapeutic metallacycle **8** (Fig. 3A) for image-guided cancer radiochemotherapy, and it has a long wavelength perylene bisimide fluorophore (PPy) and metal–organic precursor (TPE–Pt) as

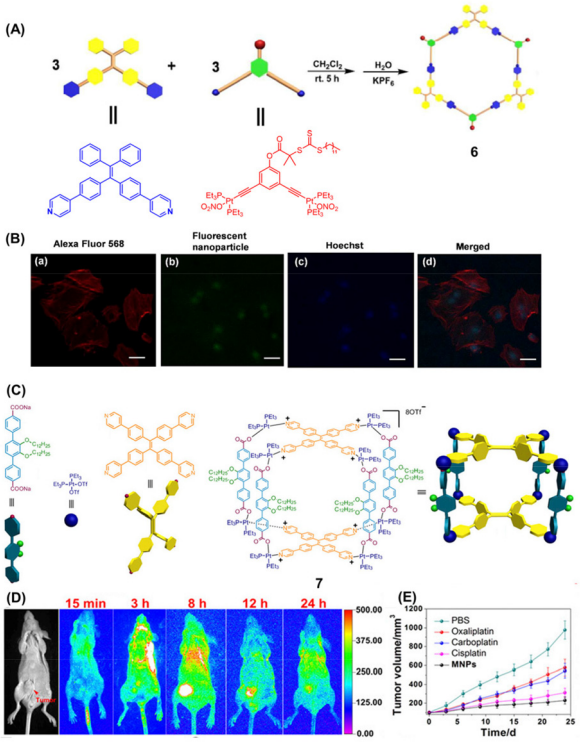

Fig. 2 (A) Structure of Pt(II) metallacycle **6**; (B) CLSM of BMSC cells incubated with metallacycle **6** for 6 h; the cell cytoskeleton was stained for the actin filament using Alexa Fluor 568 phalloidin (red), the cell nucleus was stained using DAPI (blue), and green fluorescence indicates the presence of **6** (scale bar = 50 μm), the figure adapted from ref. 23 with permission from the Royal Society of Chemistry, Copyright 2017; (C) structure of Pt(II) metallacage **7**; (D) *in vivo* fluorescence imaging of mice following i.v. injection of **7** at different times; (E) tumor growth inhibition curves for different treatment methods on the HeLa tumor model; the figure adapted from ref. 24 with permission from the National Academy of Sciences, Copyright 2016.

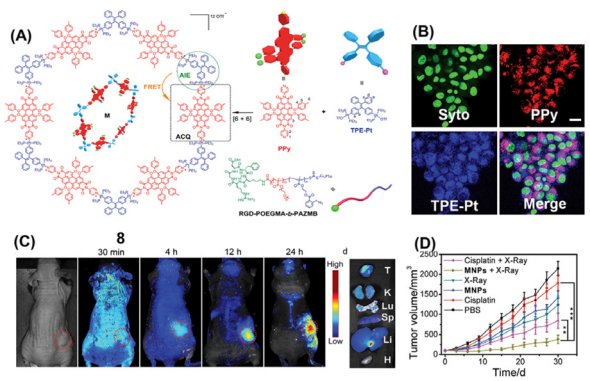

Fig. 3 (A) Structure of metallacycle **8**; (B) CLSM images of A2780 cells treated with **8** for 4 h, scale bar: 25 μm; (C) *in vivo* fluorescence imaging of macrocycle **8** at different times and the organ distribution of drugs; (D) tumor inhibition of **8**-MNPs and different control groups; the figure adapted from ref. 25 with permission from Wiley, Copyright 2022.

components.[25] The formation of this discrete supramolecular coordination complex facilitated the encapsulation of **8** by glutathione (GSH)-reactive amphiphilic block copolymers,

resulting in the preparation of **8**-loaded nanoparticles (MNPs). The near-infrared emission of PPy was used to detect the intracellular transport and tissue distribution of MNPs in real time (Fig. 3B). *In vitro* and *in vivo* studies showed that the combination of chemotherapy and radiotherapy had excellent anticancer effects. The administration of this nanodrug effectively inhibited tumor growth and greatly prolonged the survival of mice with cisplatin-resistant A2780cis tumors. Precise radiochemotherapy guided by *in vivo* fluorescence imaging (Fig. 3C) facilitated improved treatment outcomes (Fig. 3D) and minimized unwanted side effects.

2.2. Porphyrin-based metallacycles/metallacages for cancer imaging and therapy

Compared with TPE, porphyrin, which can be used as a functional group by itself, seems to have more advantages. As first-generation photosensitizers developed in the early 1980s, porphyrins are a class of macrocyclic pigments composed of four pyrroles and have broad absorption bands, the ability to chelate metal ions, and the function of photosensitizers. Their application has been expanded to the field of disease treatment and imaging.[26] However, the large π-conjugation of planar porphyrins always suffers from severe π–π stacking, resulting in significant quenching of excited states and thus a decrease in the quantum yield (QY) of $^1O_2$ production, which limits porphyrins in terms of imaging and photodynamic therapy applications. The metal–organic macrocycles/cages formed by a synergistic self-assembly strategy with metal receptors can effectively solve the above problems.

In photodynamic therapy, although reactive oxygen species can achieve efficient and drug-resistant tumor tissue ablation, non-specific light damage to normal tissues by ROS is still unavoidable. Therefore, designing photosensitizers that can specifically respond in tumor tissues and realize accurate non-invasive spatiotemporal control of ROS, to some extent, can effectively reduce the side effects of ROS and improve the therapeutic efficiency of PDT. In 2019, Yang's group successfully constructed a supramolecular system **9** (Fig. 4A) with the ability to reversibly control the generation of $^1O_2$.[27] By incorporating porphyrin and diolefin groups into the ligand-driven self-assembled building blocks of the metallacycle, the excellent photoisomerization properties of the diolefin allowed the resulting metallacycle to act as a supramolecular switch to fine-tune the generation efficiency of $^1O_2$. *In vivo* studies showed that the ring-opened form of O-NPs significantly generated phototoxicity to tumors under light, while the ring-closed form of C-NPs only slightly inhibited the growth of tumors.

Hypoxia has been a major obstacle in tumor imaging and treatment. So far, there have been mainly two methods for hypoxia imaging. One is the detection method of nitroreductase and azoreductase with irreversible emission of probes, and the other is the dynamic emission of phosphorescent probes with changes in O_2 concentration. Stang and Huang have prepared a dual-emitting metallacage **10** (Fig. 4B) with blue fluorescence and red phosphorescence, to which different

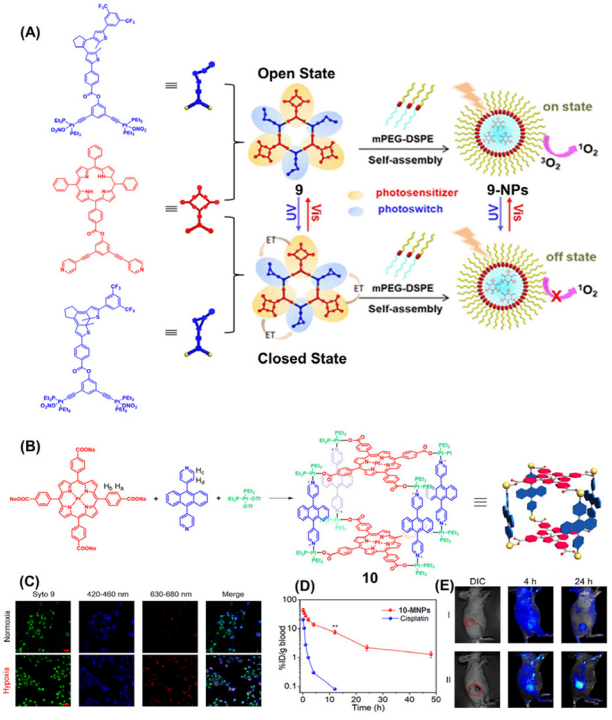

Fig. 4 (A) Structure of metallacycle **9** and the mechanism of the controllable $^1O_2$ production, the figure adapted from ref. 27 with permission from the American Chemical Society, Copyright 2019; (B) structure of metallacycle **10**; (C) CLSM images of cells stained with Syto and **10**-MNPs under normoxic or hypoxic conditions; (D) plasma platinum concentration *versus* time after injection of cPt and **10**-MNPs; (E) *in vivo* fluorescence imaging at different times of **10**-MNPs; the figure adapted from ref. 28 with permission from Wiley, Copyright 2020.

ligands can bind and it has dual-emitting ability.[28] Under hypoxia, the red phosphorescence was enhanced nearly 48-fold, while the blue fluorescence emission did not change significantly (Fig. 4C). After the formation of nanoparticles by amphiphilic chain self-assembly, the metal macrocycle showed gradually increased red phosphorescence with the reduction of oxygen. *In vitro* studies have demonstrated a phosphorescence and fluorescence ratio change with the oxygen concentration. Likewise, *in vivo* experiments have shown its better tumor accumulation ability, circulation half-life (Fig. 4D), imaging performance (Fig. 4E), and therapeutic performance. The high sensitivity, stability and anti-tumor ability of this hypoxia imaging chemotherapeutic drug have given it potential application value.

For high-precision tumor imaging, the use of multiple imaging modalities together often results in better therapeutic effects. Positron emission tomography (PET) has the advantages of high sensitivity and unlimited penetration depth, while magnetic resonance imaging (MRI) has high resolution. These two imaging techniques are often used together due to their better complementarity.[29] Chen *et al.* prepared a complex porphyrin-based metallacage **11** (Fig. 5A) from a porphyrin derivative,[30] terephthalic acid and 90° platinum using a multi-component ligand-driven self-assembly strategy. *In vitro*

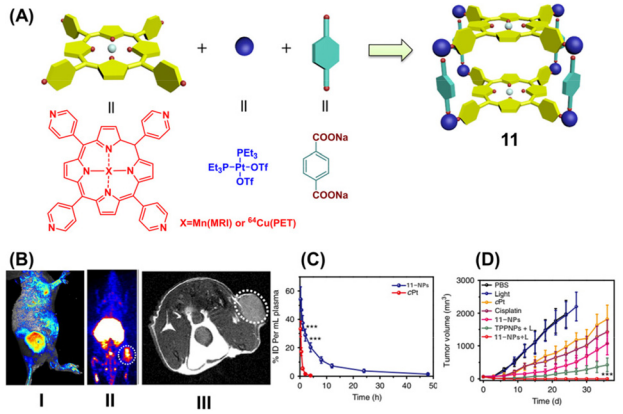

Fig. 5 (A) Structure of metallacycle **11**; (B) the use of **11** for *in vivo* NIR/PET/MRI multimodal imaging of tumor-bearing nude mice; (C) plasma platinum concentration *versus* time after injection of cPt and **11**-MNPs; (D) tumor volume inhibition in different control groups and those treated with **11**-NPs; the figure is adapted from ref. 30 with permission from Springer Nature, Copyright 2018.

studies showed that **11**-NPs can target αvβ3 integrin receptor-overexpressing cells and were then taken up by cells and eventually trapped in lysosomes, with excellent ROS generation capacity under 671 nm laser irradiation. Pt coordinated with N7 atoms on purine bases to form intra- and inter-strand crosslinks on DNA and PDT oxidized DNA or protein in cells, which significantly increased the cell death rate to 95.6%. In addition to *in vivo* fluorescence imaging, **11**-NPs can also act as contrast agents in MRI or PET after chelating Mn^{2+} or ^{64}Cu ions, and multimodal imaging can enable comprehensive diagnosis of cancer (Fig. 5B). After a single-dose injection into tumor model mice, **11**-NPs showed high tumor enrichment and a long blood circulation half-life (Fig. 5C). Moreover, owing to synergistic photochemotherapy, excellent tumor suppression without recurrence (Fig. 5D) as well as excellent anti-metastatic effects and low side effects on normal tissues are achieved.

2.3. BODIPY-based metallacycles/metallacages for cancer imaging and therapy

Compared with TPE and porphyrin fluorophores, BODIPY-based organic frameworks have potential D–A–D structures, and by introducing different groups on the BODIPY core, its emission wavelength can even be adjusted to the near-infrared region, which is more propitious for accurate imaging *in vivo*.[31] Furthermore, due to its large molar extinction coefficient, high fluorescence quantum yield, relatively long excited state lifetime and remarkable photostability, BODIPY has been adopted in various fields such as bioimaging, photodynamic therapy (PDT) and photothermal therapy (PTT).[32] However, due to its low water solubility and severe ACQ effect, it suffered setbacks in biological experiments. The lower intersystem crossing (ISC) efficiency of BODIPY makes its single-linear state oxygen generation capacity extremely low, which is fatal in the PDT field. Fortunately, the formation of metal macrocycles, on the one hand, suppresses the π–π stacking between fluorophores. On the other hand, it can utilize the heavy atom effect of metals to improve the ISC efficiency, thereby promoting the generation of singlet oxygen. In addition, the solubility of the complexes in organisms is somewhat improved.

In 2013, four macrocycles **12–15** (Fig. 6A) with pyridine functionalized BODIPY as an organic ligand and half sandwich complexes Ru(II) and Ir(III) as receptors were synthesized by Lee *et al.*[33] *In vitro* cell experiments showed that some of the complexes were more cytotoxic to MCF-7 and U87 cells than cisplatin (Fig. 6B). The cytotoxicity of these metal complexes increased with the number of benzene in the half-sandwich receptor, which the authors attributed to the increased electron density on the metal nuclei favoring ligand exchange, stabilization of higher oxidation states and improved oxidation capacity. Further studies showed that these metal macrocycles can induce late apoptosis and induce cell cycle arrest in both the S phase and G2/M phases (Fig. 6C). The typical absorption peaks of salmon sperm DNA around 260 nm showed a signifi-

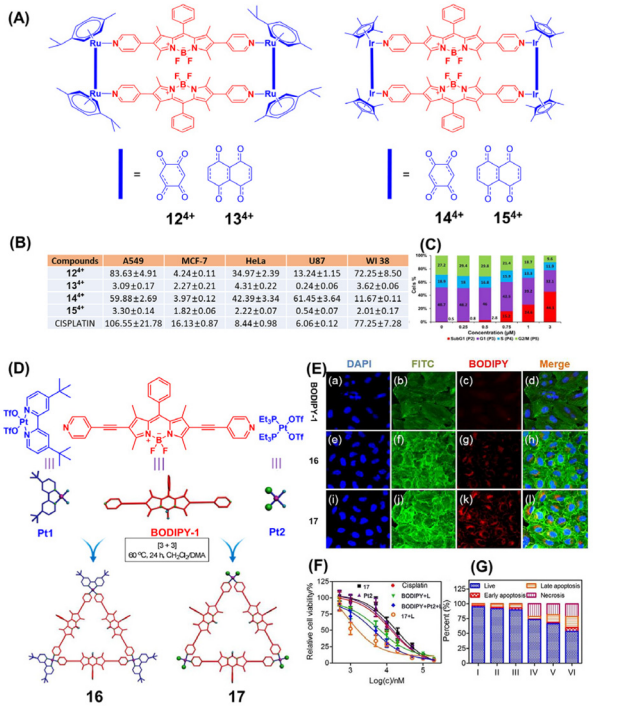

Fig. 6 (A) Structures of metallacycles **12–15**; (B) IC_{50}(μM) of metallacycles **12–15** and cisplatin in different cell lines; (C) graphical representation of cell cycle analysis of metallacycle **15** treated U87 cells; the figure is adapted from ref. 33 with permission from the Royal Society of Chemistry, Copyright 2016; (D) structures of metallacycles **16** and **17**; (E) CLSM images of HeLa cells after incubation with the ligand BODIPY-1 and metallacycles **16** and **17** for 8 h; (F) cytotoxicity of different formulations against drug resistant A2780cis cells; (G) flow-cytometric analysis of HeLa cells after different treatments (I: **16**, II: Pt2, III: cisplatin, IV: BODIPY-1 + L, V: BODIPY-1 + Pt2 + L, VI: **17** + L); the figure is adapted from ref. 34 with permission from the American Chemical Society, Copyright 2018.

cant concentration-dependent hyperchromic shift behaviour with the addition of these macrocycles.

BODIPY-based highly emissive Pt(II) supramolecular triangles **16** and **17** (Fig. 6D) prepared by Huang's group had a better combined phototherapy–chemotherapy effect.[34] These metal macrocycles showed good anticancer activity against HeLa cells (IC_{50} of 6.41 μM (**16**) and 2.11 μM (**17**)). Because of the negative potential of the cell membrane, confocal fluorescence microscopy showed that the cationic macrocycle had a faster uptake rate and higher intracellular accumulation (Fig. 6E). *In vitro* studies have shown that the metal rings have extremely low IC_{50} values (0.76 μM) against drug-resistant A2780cis cells under 400–700 nm laser irradiation, which is up to an order of magnitude more potent than chemotherapy alone, and their cytotoxicity is approximately 9-fold higher than that of FDA-approved cisplatin. Moreover, the combination index was calculated to be 0.843, which validated their significant synergistic effect (Fig. 6F) and showed that the mode of cell death was mainly late apoptosis (Fig. 6G).

The development of drugs with high stability and strong absorption in the NIR region is essential to provide deep tissue penetration capabilities and effective therapeutic properties.[35] Additionally, the metallacycles located in the NIR is benefit for local non-invasive photothermal therapy (PTT), which converts NIR light energy into thermal energy for cancer cell inhibition.[36] Zhao's group synthesized a class of BODIPY–Pt metal macrocycles **18–20** (Fig. 7A) modified with alkyne bonds to integrate chemotherapy, photodynamic therapy and photothermal therapy as an integrated treatment platform, with strong absorption at 650–800 nm.[37] The spin–orbit coupling effect of Pt improved the triplet-state excitation lifetime and the single-linear state oxygen quantum yield of MNPs. Compared with cyanine dyes and gold nanorods, they had superior photothermal conversion efficiency (*i.e.*, **18**-NPs (27.7%), **19**-NPs (28.3%), and **20**-NPs (31.1%)), which was attributed to the Pt-promoted enhancement of non-radiative transformation. Flow cytometry indicated that cell death was mainly due to late apoptosis induced by synergistic PDT/PTT. After intravenous injection into mice, 785 nm laser treatment at a power of 0.5 Wcm^{-2} presented objective photothermal imaging effects (Fig. 7B), and the tumor volume reduction in the combined treatment group was quite significant compared with the control group (Fig. 7C).

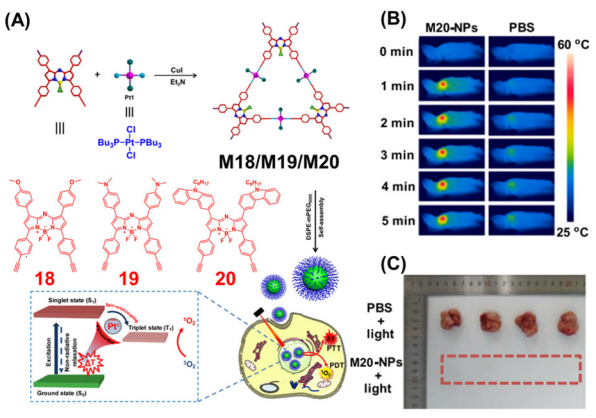

Fig. 7 (A) Structures of metallacycles **18–20**; (B) photothermal imaging of mice in the control group and **M20**-NP group; (C) tumor volume inhibition in the control group and **M20**-NP group; the figure is adapted from ref. 37 with permission from the American Chemical Society, Copyright 2020.

2.4. NIR-II dye based metallacycles/metallacages for cancer imaging and therapy

The above-mentioned organic fluorophores are all located in the traditional fluorescence imaging window (0.4–0.9 μm). The poor tissue penetration ability, low signal to background ratio (SBR) and low imaging resolution of tumors may lead to the deviation between the imaging feedback and the actual treatment effect. Fluorescence imaging in the NIR-II (1–1.7 μm) window has the advantages of significantly reduced photon scattering and absorption, lower tissue autofluorescence, greater tissue penetration, and better spatial and temporal resolution.[38] In 2009, Dai's team used single-walled carbon nanotubes (SWCTNs) to achieve the first NIR-II window fluorescence imaging of living tumor blood vessels. Following this work, NIR-II fluorescence imaging technology emerged and has been used in the biomedical field and other scientific research areas.[39]

Since the discovery of SWCTNs, small molecule NIR-II dyes have attracted much attention due to their rapid metabolism *in vivo*, high biocompatibility and diverse modifiable sites. Due to the high-quality *in vivo* imaging characteristics of NIR-II dyes, NIR-II dyes and therapeutic metal-drugs are encapsulated in nanoparticles, which can achieve a high signal-to-noise ratio and can monitor the therapeutic effect of

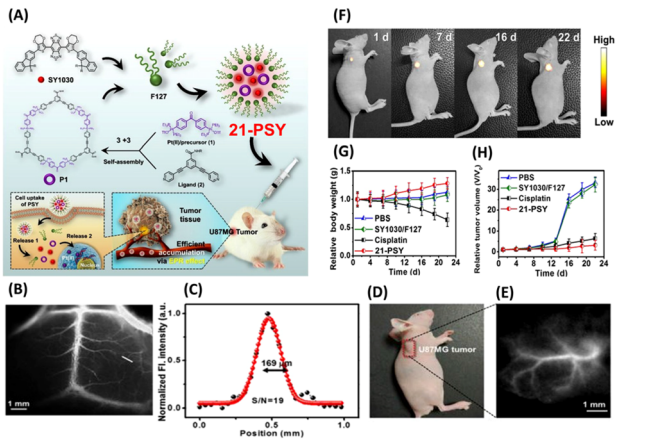

Fig. 8 (A) Depiction of **21**-PSY nanocomplex preparation and illustration of the cellular uptake and Pt(II) release from **21**-PSY; (B) NIR-II images of brain vessels; (C) the width and SBR of NIR-II images of brain vessels; (D and E) U87MG tumor blood vessel images; (F) monitoring the **21**-PSY therapeutic response in U87MG tumors; (G) average body weights were analyzed; (H) U87MG tumor growth inhibition curves for PBS, cisplatin, SY1030 and **21**-PSY. Reproduced with permission from ref. 40, Copyright 2019, Royal Society of Chemistry.

the metal-drugs in real time. In 2019, Kim and Sun successfully constructed **21**-PSY nanoparticles (Fig. 8A) for integrated metallacycle-based precision imaging and tumor elimination by co-encapsulating organic platinum metallacycles and NIR-II organic probes in the triblock copolymer F127.[40] They can enhance the uptake of Pt(II) in tumors and precisely monitor tumor inhibition in real time through the NIR-II fluorescence signal. The presence of NIR-II molecules endowed the nanoparticles with high photostability and quantum yield, with a penetration depth of up to 5 mm, visualization of the living circulatory system through NIR-II fluorescence signals (Fig. 8B and C), and high-resolution and precise tumor position (Fig. 8D and F). In addition, the EPR effect caused an increase in drug accumulation at the tumor site, effectively inhibited the growth of U87MG subcutaneous tumor-bearing mice and orthotopic mammary tumors (Fig. 8G), reduced adverse side effects and prolonged the survival of mice (Fig. 8H).

Taking into account the tumor elimination effect of the probe, the low targeting ability, the enrichment in normal organs, and the limitation of tumor penetration ability, Stang and Sun optimized the previous work by covalently linking endogenous melanin to the NIR-II molecule and then self-assembling with the macrocycle **22** (Fig. 9A).[41] After intravenous injection **into** U87MG tumor-bearing nude mice, fluorescence imaging and photoacoustic imaging were performed, and the tumor was clearly demarcated from the surrounding background tissue (Fig. 9B). The imaging results showed that the maximum accumulation was reached at 6 h, and the organ distribution experiment showed that the tumor targeting ability of the drug was high (Fig. 9C). Under 808 nm laser irradiation, the combined treatment of photothermal therapy and chemotherapy increased the tumor elimination ability (Fig. 9D) and showed lower side effects and prolonged the survival time of mice. These probes with precise NIR-II window imaging and targeted therapy pave the way for the researchers' follow-up work.

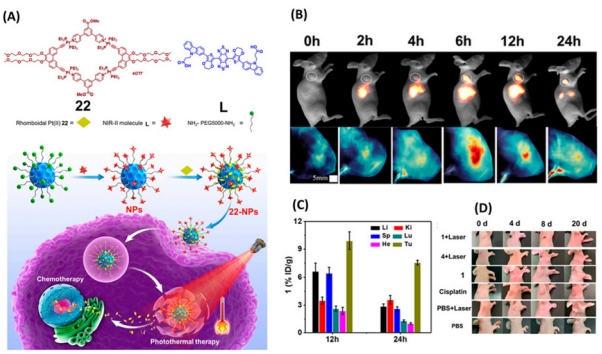

Fig. 9 (A) Depiction of **22**-NP preparation and illustration of the cellular uptake and the combination therapy; (B) NIR-II fluorescence and PA images of tumor mice at different times after tail vein injection of **22**-NPs; (C) drug distribution of **22**-NPs in different organs at 12 h and 24 h; (D) representative photographs of tumors in mice treated with different formulations. Reproduced with permission from ref. 41, Copyright 2019, National Academy of Sciences.

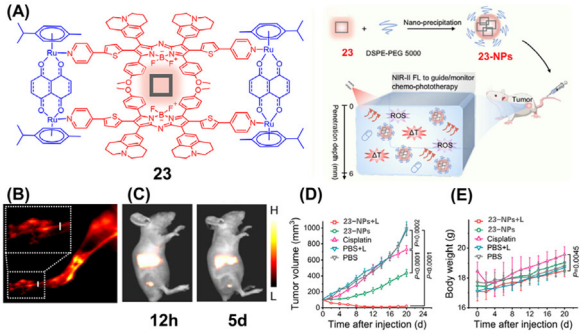

Fig. 10 (A) Structure of metallacycle **23** and the diagram of the anticancer mechanism of **23**-NPs in tumor-bearing mouse models; (B) NIR-II FI of hindlimb vessels after i.v. injection of **23**-NPs; (C) NIR-II FI of tumors at 12 h and 5 d; (D) tumor volume inhibition in different control groups and the **23**-NP group; (E) mouse health status after treatment with different control groups; reproduced with permission from ref. 42. Copyright 2022, Springer Nature.

Due to the complexity of the physiological environment, the simultaneously encapsulated nanoparticles with a therapeutic metallacycle and imaging NIR-II dye may lack precise spatiotemporal uniformity, resulting in poor therapeutic effects for real-time detection. Based on this problem, our group synthesized a metal–organic macrocycle **23** (Fig. 10A) with excellent real-time monitoring ability through the coordination self-assembly of meticulously designed azo-BODIPY-based NIR-II dye molecules and semi-sandwich ruthenium in methanol.[42] This metal macrocycle had an excitation wavelength of 808 nm and an emission wavelength of over 1085 nm, with a respectable penetration depth (~6 mm). Macrocycle **23** had a good ROS generation ability and high photothermal conversion efficiency (30.9%) and showed outstanding cellular uptake ability and ideal anticancer activity against various cancer cell lines, especially against cisplatin resistant A549 cells. Further studies revealed that macrocycle **23** induced the overexpression of caspase 3/7 and mitochondrion-mediated apoptosis while arresting the cell cycle in the S phase and G2/M phase. *In vivo* studies showed that under excitation with 808 nm light, high-resolution hindlimb vascular imaging (Fig. 10B) and obvious tumor contours (SBR > 4, duration: 12–120 h) were observed (Fig. 10C). With regard to metal–organic macrocycle **23**, precise NIR-II fluorescence imaging guided and long-term monitored chemo-phototherapy showed superior A549 tumor ablation (Fig. 10D) compared to cisplatin as well as very few side effects (Fig. 10E).

3. Discussion

In this review, we give an account of the application of metallacycles/metallacages with high fluorescence emission properties formed by a coordination driven self-assembly strategy in tumor imaging and therapy. Accurate imaging techniques require the ability to monitor and analyze physiological processes *in vivo* with high spatial resolution. TPE is the star mole-

cule in the constructed metal macrocycle/cage system due to its better AIE properties, easy functionalization, and highly symmetric structure, but obtaining high quality imaging in organisms still requires a bathochromic shift of the absorption/emission to the near-infrared region, which is difficult with only TPE emitting ligands in the backbone. Porphyrins can easily red-shift to the near-infrared region through chelating some transition metals, especially lanthanides, which facilitates accurate imaging in organisms.[43] In the past decade, metallacycle/metallacage species have made great progress in biomedical applications; however, research on formulations based on them for biomedicine is still in its infancy and many challenges remain before clinical applications. The multi-functional diagnosis and therapy platform that can be developed from metallacycle/metallacage species needs further research by scientists.

4. Perspective

Metallacycles/metallacages that integrate precise imaging and tumor elimination can bring better therapeutic effects. Nonetheless, the current research field is largely stuck in the visible region, which gives poor imaging results. Due to the complexity of the intra-biological environment, the formation of supramolecular species of fixed shape and size of metal drugs followed by co-encapsulation with NIR II organic fluorescent small molecules in amphiphilic polymers may result in imprecise spatio-temporal unification of imaging and therapeutic components.[44] The introduction of NIR-II organic fluorescent molecules directly into the metallacycle/metallacage backbone may lead to better diagnostic–therapeutic results. Metallacycles/metallacages based on the NIR-II region have been reported in the past few years, which better solve the problems of tumor penetration depth and imaging spatial and temporal resolution.[45] However, only a few types of organic small molecules in the near-infrared second region have been developed – anthocyanins, D–A–D, azo-BODIPY and so on. In the future, it is necessary to explore more NIR-II organic skeletons to build more exquisite metallacycles/metallacages to achieve an integrated platform for accurate imaging and multifunctional cooperative therapy.

Most of the metallacycles/metallacages can effectively solve the problems of water solubility, stability and targeting through encapsulation in some amphiphilic block compounds. Additionally, the excellent EPR effect with the appropriate size of nanoparticles (100–200 nm) can result in a highly permeable tumor vasculature and impaired lymphatic drainage. However, although the EPR effect is regarded as the main mechanism of nanomedicine, the reliability of EPR in large animal or human tumors is still highly controversial.[46] The blood flow in normal human organs is approximately 800 times faster than that in normal mouse organs. This difference may explain why nanodrugs accumulate better in rodent solid tumors than in human solid tumors.[47] In addition, the problem of low therapeutic efficacy may be caused by the impairment of tumor cell inhibition properties by the polyethylene glycolization of liposomes, while the EPR effect may be a secondary factor.[48] In a nut shell, EPR effects may not be a universal feature in all species and the issue of heterogeneity among tumors remains to be addressed.[49] Until now, there are some existing or emerging approaches which may be alternative tumor-targeted delivery mechanisms, including endogenous cell carriers, non-immunogenic bacteria-mediated delivery and the trans-endothelial pathway.[50]

In the research of metal drugs for tumor ablation, at present, the most studied is the cell death caused by the binding of heavy metals (Pt, Pd, Ru, *etc.*) to DNA bases. However, based on recent studies, scientists have found that the chemotherapy process includes cisplatin-induced normal tissue damage and weight loss, possibly due to caspase-3 activation of GSDME-mediated thermal apoptosis in normal tissues.[51] In addition, there is evidence that some chemo-platinum complexes induce immunogenic cell death.[52] It can be seen that the anticancer behaviour of metal drugs may be caused by multiple mechanisms. Further research on these mechanisms may eliminate the shortcomings of systemic toxicity and resistance to metal drugs during chemotherapy.

In a nutshell, metal drugs have been used in cancer treatment for more than 40 years, and the serious side effects, drug resistance, and delivery methods associated with first-generation drugs are being improved and solved by researchers, which is key to clinical transformation. The metallacycles formed by synergistic self-assembly can achieve the effect of "1 + 1 > 2" by combining the functions of different components. The introduction of organic ligands with excellent fluorescence properties, especially NIR-II dye molecules, endows metallacycles with high spatiotemporal resolution imaging performance, which greatly improves the efficiency of tumor therapy. These luminescent organometallic complexes enrich the application of supramolecular drugs in cancer therapy.

Abbreviations

ACQ	Aggregation caused quenching
AIE	Aggregation-induced emission
A2780	Human ovarian carcinoma cell line
A549	Human lung cancer cell line
BODIPY	Difluoroboron dipyrromethenes
CLSM	Confocal laser scanning microscope
D–A–D	Donor–acceptor–donor
EPR	Enhanced permeability and retention
FDA	Food and Drug Administration
FI	Fluorescence imaging
GSH	Glutathione
HeLa	Human adenocarcinoma of the cervix cell line
HepG-2	Human hepatocarcinoma cell line
IC50	Half maximal inhibitory concentration
ISC	Intersystem crossing
IV	Intravenous injection
MCF-7	Human breast carcinoma cell line

mPEG-DSPE	1,2-Distearoyl-*sn-glycero*-3 phosphoethanolamine-*N*-[methoxy(polyethylene glycol)]
MRI	Magnetic resonance imaging
NIPAAM	*N*-Isopropylacrylamide
NIR	Near-infrared
NPs	Nanoparticles
PDT	Photodynamic therapy
PET	Positron emission tomography
PPy	Perylene bisimide
PTT	Photothermal therapy
QY	Quantum yield
ROS	Reactive oxygen species
SBR	Signal-to-background ratio
SBR	Signal-to-noise ratio
SCCs	Supramolecular coordination complexes
SWCNTs	Single-walled carbon nanotubes
TPE	Tetraphenylethylene
U87	Human glioma cell line

Conflicts of interest

There are no conflicts to declare.

Acknowledgements

This work is supported by the National Natural Science Foundation of China (22022404, 22074050), Hubei Provincial Central Leading Local Science and Technology Development Fund Project (2020ZYYD002), and the Fundamental Research Funds for the Central Universities (CCNU22QN007).

References

1 H. Sung, J. Ferlay, L. Siegel, M. Laversanne, I. Soerjomataram, A. Jemal and F. Bray, *CA Cancer J. Clin.*, 2021, **71**, 209–249.

2 (*a*) Y. Qin, Q. Zhang, X. Cheng, L. Rong and Z. Zhang, *Biomaterials*, 2017, **112**, 234–247; (*b*) Q. Wu, Z. Yang, Y. Nie, Y. Shi and D. Fan, *Cancer Lett.*, 2014, **347**, 159–166; (*c*) M. Umeh-Garcia, C. Simion, Y. Ho, N. Batra, L. Berg, L. Carraway, A. Yu and C. Sweeney, *Cancer Res.*, 2020, **80**, 418–429; (*d*) C. Liang, L. Xu, G. Song and Z. Liu, *Chem. Soc. Rev.*, 2016, **45**, 6250–6269; (*e*) W. Tuo, Y. Xu, Y. Fan, J. Li, M. Qiu, X. Xiong, X. Li and Y. Sun, *Coord. Chem. Rev.*, 2021, **443**, 214017; (*f*) Y. Wang, Z. Zhang, S. Xu, F. Wang, Y. Shen, S. Huang and S. Guo, *Nanomedicine*, 2017, **13**, 1785–1795.

3 (*a*) L. Kelland, *Nat. Rev. Cancer*, 2007, **7**, 573–584; (*b*) C. Xia, J. Zhang, N. Chen, C. Cheng, D. Chu, H. Tang, Y. Li and Y. Cui, *Coord. Chem. Rev.*, 2021, **435**, 213783; (*c*) C. Bruijnincx and J. Sadler, *Curr. Opin. Chem. Biol.*, 2008, **12**, 197–206; (*d*) D. Hernández-Romero, S. Rosete-Luna, A. López-Monteon, A. Chávez-Piña, N. Pérez-Hernández, J. Marroquín-Flores, A. Cruz-Navarro, G. Pesado-Gómez, D. Morales-Morales and R. Colorado-Peralta, *Coord. Chem. Rev.*, 2021, **439**, 213930; (*e*) Q. Zhao, W. Zhang, Z. Ning, X. Zhuang, H. Lu, J. Liang, J. Li, Y. Zhang, Y. Dong, Y. Zhang, S. Zhang, S. Liu and B. Liu, *PLoS One*, 2004, **9**, e93103.

4 M. Deo, L. Ang, B. McGhie, A. Rajamanickam, A. Dhiman, A. Khoury, J. Holland, A. Bjelosevic, B. Pages, C. Gordon and R. Aldrich-Wright, *Coord. Chem. Rev.*, 2018, **375**, 148–163.

5 (*a*) D. Zhang, J. Pan, X. Xiang, Y. Liu, G. Dong, J. Livingston, K. Chen, M. Yin and Z. Dong, *J. Am. Soc. Nephrol.*, 2017, **28**, 1131–1144; (*b*) Z. Deng, N. Wang, Y. Liu, Z. Xu, Z. Wang, C. Lau and G. Zhu, *J. Am. Chem. Soc.*, 2020, **142**, 7803–7812; (*c*) K. Peng, B. Liang, T. Liu and W. Mao, *Coord. Chem. Rev.*, 2021, **449**, 214210; (*d*) R. Gust, W. Beck, G. Jaouen and H. Schönenberger, *Coord. Chem. Rev.*, 2009, **253**, 2742–2759; (*e*) L. Zhang, B. Jiang, N. Zhu, M. Tao, Y. Jun, X. Chen, Q. Wang and C. Luo, *Med. Oncol.*, 2020, **37**, 5.

6 (*a*) M. Chen, F. Zhang, D. Shao, B. Zhang, Q. Zheng, W. Wang, W. Yang, Z. Wang, J. Chen, F. Dong, N. Xiao and K. Wu, *Appl. Mater. Today*, 2020, **19**, 100558; (*b*) M. Yang, H. Zhao, Z. Zhang, Q. Yuan, Q. Feng, X. Duan, S. Wang and Y. Tang, *Chem. Sci.*, 2021, **12**, 11515–11524; (*c*) M. Lifshits, A. Roque III, P. Konda, S. Monro, D. Cole, D. von Dohlen, S. Kim, G. Deep, P. Thummel, G. Cameron, S. Gujar and A. McFarland, *Chem. Sci.*, 2020, **11**, 11740–11762.

7 A. Jayawardhana, M. Stilgenbauer, P. Datta, Z. Qiu, S. McKenzie, H. Wang, D. Bowers, M. Kurokawa and R. Zheng, *Chem. Commun.*, 2020, **56**, 10706–10709.

8 G. Kenny and J. Marmion, *Chem. Rev.*, 2019, **119**, 1058–1137.

9 Y. Lu, X. Ma, X. Chang, Z. Liang, L. Lv, M. Shan, Q. Lu, Z. Wen, R. Gust and W. Liu, *Chem. Soc. Rev.*, 2022, **51**, 5518–5556.

10 (*a*) S. Datta, L. Saha and P. J. Stang, *Acc. Chem. Res.*, 2018, **51**, 2047–2063; (*b*) R. Cook, R. Zheng and P. J. Stang, *Chem. Rev.*, 2013, **113**, 734–777; (*c*) Y. Wu, J. Chen, L. Xu, L. Zhao and H. Yang, *Coord. Chem. Rev.*, 2018, **369**, 39–75; (*d*) W. Wang, X. Wang and H. Yang, *Chem. Soc. Rev.*, 2016, **45**, 2656–2693.

11 (*a*) A. Garci, J. Castor, J. Fakhoury, L. Do, J. Di Trani, P. Chidchob, S. Stein, K. Mittermaier, T. Friscic and H. Sleiman, *J. Am. Chem. Soc.*, 2017, **139**, 16913–16922; (*b*) L. Tu, C. Li, C. Liu, S. Bai, J. Yang, X. Zhang, L. Xu, X. Xiong and Y. Sun, *Chem. Commun.*, 2022, **58**, 9068–9071.

12 (*a*) E. Paul, B. Therrien and J. Furrer, *Org. Biomol. Chem.*, 2015, **13**, 946–953; (*b*) G. Gupta, A. Das, C. Park, A. Tron, H. Kim, J. Mun, N. Mandal, W. Chi and Y. Lee, *Inorg. Chem.*, 2017, **56**, 4616–4622; (*c*) S. Datta, K. Misra, L. Saha, N. Lahiri, J. Louie, D. Pan and P. J. Stang, *Proc. Natl. Acad. Sci. U. S. A.*, 2018, **115**, 8087–8092; (*d*) J. Zhu, C. Chu, S. Li, X. Pang, L. Zheng, Q. Wang, S. Shi, Y. Zhang, Y. Cheng, E. Ren, L. Cheng, X. Chen and G. Liu, *Adv. Funct. Mater.*, 2019, **36**, 1904056.

13 (*a*) J. Xiao, L. Cheng, T. Fang, Y. Zhang, J. Zhou, R. Cheng, W. Tang, X. Zhong, Y. Lu, L. Deng, X. Cheng, Y. Zhu, Z. Liu and W. Cui, *Small*, 2019, **15**, 1904979; (*b*) H. Dai, H. Yan, F. Dong, L. Zhang, N. Du, L. Sun, N. Li, G. Yu, Z. Yang, Y. Wang and M. Huang, *Biomater. Sci.*, 2022, **10**, 1456–1069; (*c*) H. Wang, Y. Ma, H. Wang, F. Wang, T. Xu and Q. Gu, *Adv. Funct. Mater.*, 2019, **29**, 1905480.

14 (*a*) G. Lan, K. Ni, Z. Xu, S. Veroneau, Y. Song and W. Lin, *J. Am. Chem. Soc.*, 2018, **140**, 5670–5673; (*b*) L. Li, C. Shao, T. Liu, Z. Chao, H. Chen, F. Xiao, H. He, Z. Wei, Y. Zhu, H. Wang, X. Zhang, Y. Wen, B. Yang, F. He and L. Tian, *Adv. Mater.*, 2020, **32**, 2003471; (*c*) Y. Xi, X. Xie, Y. Peng, P. Liu, J. Ding and W. Zhou, *Nanoscale*, 2021, **13**, 5125–5135.

15 (*a*) Y. Sun, C. Chen, J. Liu and P. J. Stang, *Chem. Soc. Rev.*, 2020, **49**, 3889–3919; (*b*) Y. Xu, C. Li, X. Ma, W. Tuo, L. Tu, X. Li, Y. Sun, P. J. Stang and Y. Sun, *Proc. Natl. Acad. Sci. U. S. A.*, 2022, **119**, e2209904119.

16 Z. Yue, H. Wang, Y. Li, Y. Qin, L. Xu, J. Bowers, M. Gangoda, X. Li, B. Yang and R. Zheng, *Chem. Commun.*, 2018, **54**, 731–734.

17 N. Singh, S. Jang, J. H. Jo, D. H. Kim, D. W. Park, I. Kim, H. Kim, S. C. Kang and K. W. Chi, *Chemistry*, 2016, **22**, 16157–16164.

18 Z. Zhou, J. Liu, T. W. Rees, H. Wang, X. Li, H. Chao and P. J. Stang, *Proc. Natl. Acad. Sci. U. S. A.*, 2018, **115**, 5664–5669.

19 P. d. Boissieu, *J. Chem. Soc.*, 1888, **54**, 928–972.

20 Q. Dong, Y. Lam, J. Qin, Z. Liu, Z. Li, B. Tang, X. Sun and S. Kwok, *Appl. Phys. Lett.*, 2007, **91**, 011111.

21 (*a*) J. Li, J. Wang, H. Li, N. Song, D. Wang and B. Tang, *Chem. Soc. Rev.*, 2022, **49**, 1144–1172; (*b*) Y. Zhang, X. Zhang, H. Yang, L. Yu, Y. Xu, A. Sharma, P. Yin, X. Li, J. S. Kim and Y. Sun, *Chem. Soc. Rev.*, 2021, **50**, 11227–11248.

22 B. Cheng, Y. Li, B. Tang and J. Yoon, *Chem. Soc. Rev.*, 2020, **49**, 21–31.

23 W. Zheng, G. Yang, T. Jiang, N. Shao, Q. Yin, L. Xu, P. Li, S. Chen and H. Yang, *Mater. Chem. Front.*, 2017, **1**, 1823–1828.

24 G. Yu, R. Cook, Y. Li, X. Yan, D. Wu, L. Shao, J. Shen, G. Tang, F. Huang, X. Chen and P. J. Stang, *Proc. Natl. Acad. Sci. U. S. A.*, 2016, **113**, 13720–13725.

25 Y. Ding, Z. Tong, L. Jin, B. Ye, J. Zhou, Z. Sun, H. Yang, L. Hong, F. Huang, W. Wang and Z. Mao, *Adv. Mater.*, 2022, **34**, 2106388.

26 Q. Jin, V. Chau, F. Arambula, S. Gao, L. Sessler and L. Zhang, *Chem. Soc. Rev.*, 2022, **51**, 6177–6209.

27 Y. Qin, L. Chen, F. Dong, S. Jiang, G. Yin, X. Li, Y. Tian and H. Yang, *J. Am. Chem. Soc.*, 2019, **141**, 8943–8950.

28 H. Zhu, Q. Li, B. Shi, F. Ge, Y. Liu, Z. Mao, H. Zhu, S. Wang, G. Yu, F. Huang and P. J. Stang, *Angew. Chem., Int. Ed.*, 2020, **59**, 20208–20214.

29 (*a*) K. Heinzmann, L. M. Carter, J. S. Lewis and E. O. Aboagye, *Nat. Biomed. Eng.*, 2017, **1**, 697–713; (*b*) J. Kim, Y. Piao and T. Hyeon, *Chem. Soc. Rev.*, 2009, **38**, 372–390; (*c*) K. Heinzmann, L. Carter, J. Lewis and E. Aboagye, *Nat. Biomed. Eng.*, 2007, **1**, 697–713.

30 G. Yu, S. Yu, M. Saha, J. Zhou, T. Cook, B. Yung, J. Chen, Z. Mao, F. Zhang, Z. Zhou, Y. Liu, L. Shao, S. Wang, C. Gao, F. Huang, P. J. Stang and X. Chen, *Nat. Commun.*, 2018, **9**, 4335.

31 (*a*) Y. Qin, X. Liu, P. Jia, L. Xu and H. Yang, *Chem. Soc. Rev.*, 2020, **49**, 5678–5703; (*b*) A. Turksoy, D. Yildiz and E. Akkaya, *Coord. Chem. Rev.*, 2019, **379**, 47–64; (*c*) F. Li, J. Yin and G. Kuang, *Coord. Chem. Rev.*, 2021, **448**, 214157.

32 (*a*) W. Sun, X. Zhao, J. Fan, J. Du and X. Peng, *Small*, 2019, **15**, 1804927; (*b*) S. Qi, N. Kwon, Y. Yim, V. Nguyen and J. Yoon, *Chem. Sci.*, 2020, **11**, 6479–6484; (*c*) Z. Wang, L. Huang, Y. Yan, A. El-Zohry, A. Toffoletti, J. Zhao, A. Barbon, B. Dick, O. Mohammed and G. Han, *Angew. Chem., Int. Ed.*, 2020, **59**, 16114–16121.

33 G. Gupta, A. Das, N. Ghate, T. Kim, J. Ryu, J. Lee, N. Mandal and C. Lee, *Chem. Commun.*, 2016, **52**, 4274–4277.

34 J. Zhou, Y. Zhang, G. Yu, M. R. Crawley, A. Friedman, S. Sengupta, J. Sun, Q. Li, F. Huang and T. Cook, *J. Am. Chem. Soc.*, 2018, **140**, 7730–7736.

35 (*a*) J. Zou, P. Wang, Y. Wang, G. Liu, Y. Zhang, Q. Zhang, J. Shao, W. Si, W. Huang and X. Dong, *Chem. Sci.*, 2019, **10**, 268–276; (*b*) D. Wang, H. Su, R. Kwok, X. Hu, H. Zou, Q. Luo, M. Lee, W. Xu, J. Lam and B. Tang, *Chem. Sci.*, 2018, **9**, 3685–3693; (*c*) J. Ni, P. Zhang, T. Jiang, Y. Chen, H. Su, D. Wang, Z. Yu, R. Kwok, Z. Zhao, J. Lam and B. Tang, *Adv. Mater.*, 2018, **30**, 1805220; (*d*) X. Lin, F. Chen, X. Yu, H. Wang, H. Qiu, Y. Li, S. Yin and P. J. Stang, *Proc. Natl. Acad. Sci. U. S. A.*, 2022, **119**, e2203994119.

36 (*a*) J. Huang, B. He, Z. Zhang, Y. Li, M. Kang, Y. Wang, K. Li, D. Wang and B. Tang, *Adv. Mater.*, 2020, **32**, 2003382; (*b*) J. Xie, T. Fan, J. Kim, Y. Xu, Y. Wang, W. Liang, L. Qiao, Z. Wu, Q. Liu, W. Hu, N. Yin, L. Yang, L. Liu and J. S. Kim, *Adv. Funct. Mater.*, 2020, **30**, 2003891; (*c*) F. Zhang, G. Lu, X. Wen, F. Li, X. Ji, Q. Li, M. Wu, Q. Cheng, Y. Yu, J. Tang and L. Mei, *J. Controlled Release*, 2020, **326**, 131–139.

37 G. Li, X. Zhang, W. Zhao, W. Zhao, F. Li, K. Xiao, Q. Yu, S. Liu and Q. Zhao, *ACS Appl. Mater. Interfaces*, 2020, **12**, 20180–20190.

38 (*a*) D. Li, Q. Liu, Q. Qi, H. Shi, E. C. Hsu, W. Chen, W. Yuan, Y. Wu, S. Lin, Y. Zeng, Z. Xiao, L. Xu, Y. Zhang, T. Stoyanova, W. Jia and Z. Cheng, *Small*, 2020, **16**, 2003851; (*b*) Y. Wang, Y. Li, Z. Zhang, L. Wang, D. Wang and B. Tang, *Adv. Mater.*, 2021, **33**, 2103748; (*c*) T. Ren, Z. Y. Wang, Z. Xiang, P. Lu, H. Lai, L. Yuan, X. Zhang and W. Tan, *Angew. Chem., Int. Ed.*, 2021, **60**, 800–805; (*d*) C. Ou, W. Na, W. Ge, H. Huang, F. Gao, L. Zhong, Y. Zhao and X. Dong, *Angew. Chem., Int. Ed.*, 2021, **60**, 8157–8163; (*e*) W. Huang, H. Yang, Z. Hu, Y. Fan, X. Guan, W. Feng, Z. Liu and Y. Sun, *Adv. Healthcare Mater.*, 2021, **10**, 2101003; (*f*) P. Wang, H. Yang, C. Liu, M. Qiu, X. Ma, Z. Mao, Y. Sun and Z. Liu, *Chin. Chem. Lett.*, 2021, **32**, 168–178.

39 (*a*) K. Welsher, Z. Liu, S. P. Sherlock, J. T. Robinson, Z. Chen, D. Daranciang and H. Dai, *Nat. Nanotechnol.*, 2020, **4**, 773–780; (*b*) Y. Liu, Y. Li, S. Koo, Y. Sun, Y. Liu, X. Liu, Y. Pan, Z. Zhang, M. Du, S. Lu, X. Qiao, J. Gao, X. Wang, Z. Deng, X. Meng, Y. Xiao, J. S. Kim and X. Hong, *Chem. Rev.*, 2020, **122**, 209–268; (*c*) F. Yang, Q. Zhang, S. Huang and D. Ma, *J. Mater. Chem. B*, 2020, **8**, 7856–7879; (*d*) X. Zhang, C. Li, Y. Zhang, X. Guan, L. Mei, H. Feng, J. Li, L. Tu, G. Feng, G. Deng and Y. Sun, *Adv. Funct. Mater.*, 2022, **32**, 2207259.

40 F. Ding, Z. Chen, W. Y. Kim, A. Sharma, C. Li, Q. Ouyang, H. Zhu, G. Yang, Y. Sun and J. S. Kim, *Chem. Sci.*, 2019, **10**, 7023–7028.

41 Y. Sun, F. Ding, Z. Chen, R. Zhang, C. Li, Y. Xu, Y. Zhang, R. Ni, X. Li, G. Yang, Y. Sun and P. J. Stang, *Proc. Natl. Acad. Sci. U. S. A.*, 2019, **116**, 16729–16735.

42 Y. Xu, C. Li, S. Lu, Z. Wang, S. Liu, X. Yu, X. Li and Y. Sun, *Nat. Commun.*, 2022, **13**, 2009.

43 G. Jin, C. Chau, J. Arambula, S. Gao, J. Sessler and J. Zhang, *Chem. Soc. Rev.*, 2022, **51**, 6177–6209.

44 (*a*) Y. Sun, F. Ding, Z. Zhou, C. Li, M. Pu, Y. Xu, Y. Zhan, X. Lu, H. Li, G. Yang, Y. Sun and P. J. Stang, *Proc. Natl. Acad. Sci. U. S. A.*, 2019, **116**, 1968–1973; (*b*) L. Li, X. Dong, J. Li and J. Wei, *Dyes Pigm.*, 2020, **183**, 108756; (*c*) F. Ding, Y. Fan, Y. Sun and F. Zhang, *Adv. Healthcare Mater.*, 2019, **8**, 1900260; (*d*) X. Zeng, Y. Xiao, J. Lin, S. Li, H. Zhou, J. Nong, G. Xu, H. Wang, F. Xu, J. Wu, Z. Deng and X. Hong, *Adv. Healthcare Mater.*, 2018, **7**, 1800589; (*e*) S. Zhu, R. Tian, A. L. Antaris, X. Chen and H. Dai, *Adv. Mater.*, 2019, **31**, 1900321.

45 (*a*) Y. Fan, C. Li, S. Bai, X. Ma, J. Yang, X. Guan and Y. Sun, *Small*, 2022, **18**, 2201625; (*b*) C. Li, Y. Xu, L. Tu, M. Choi, Y. Fan, X. Chen, J. L. Sessler, J. S. Kim and Y. Sun, *Chem. Sci.*, 2022, **13**, 6541–6549; (*c*) Y. Qin, X. Chen, Y. Gui, H. Wang, B. Tang and D. Wang, *J. Am. Chem. Soc.*, 2022, **144**, 12825–12833.

46 (*a*) J. Wu, *J. Pers. Med.*, 2021, **11**, 771–779; (*b*) F. Danhier, *J. Controlled Release*, 2016, **244**, 108–121; (*c*) K. Park, *J. Controlled Release*, 2013, **172**, 391; (*d*) M. Björnmalm, J. Thurecht, M. Michael, M. Scott and F. Caruso, *ACS Nano*, 2017, **11**, 9594–9613.

47 (*a*) J. Tee, L. Yip, S. Tan, S. Santitewagun, A. Prasath, P. Ke, H. Ho and D. Leong, *Chem. Soc. Rev.*, 2019, **48**, 5381–5407; (*b*) M. Izci, C. Maksoudian, B. Manshian and S. Soenen, *Chem. Rev.*, 2021, **121**, 1746–1803; (*c*) S. Leporatti, *J. Pers. Med.*, 2022, **12**, 1259–1261; (*d*) H. Maeda, *Adv. Drug Delivery Rev.*, 2015, **91**, 3–6; (*e*) Y. Ding, Y. Xu, W. Yang, P. Niu, X. Li, Y. Chen, Z. Li, Y. Liu, Y. An, Y. Liu, W. Shen and L. Shi, *Nano Today*, 2020, **35**, 100970.

48 (*a*) J. Nichols and Y. Bae, *J. Controlled Release*, 2014, **190**, 451–464; (*b*) J. Hare, T. Lammers, M. Ashford, S. Puri, G. Storm and S. Barry, *Adv. Drug Delivery Rev.*, 2017, **108**, 25–38; (*c*) J. Fang, W. Islam and H. Maeda, *Adv. Drug Delivery Rev.*, 2020, **157**, 142–160.

49 (*a*) L. Zhao, W. Yuan, J. Li, L. Yang, Y. Su, J. Peng, R. Chen, H. Phoebe Tham, H. Chen, W. Lim, H. Xiang, P. Xing, F. Li and Y. Zhao, *Adv. Funct. Mater.*, 2018, **28**, 1806162; (*b*) T. Doane and C. Burda, *Chem. Soc. Rev.*, 2012, **41**, 2885–2911; (*c*) Y. Matsumura, *Adv. Drug Delivery Rev.*, 2020, **154**, 142–150.

50 Y. Zi, K. Yang, J. He, Z. Wu, J. Liu and W. Zhang, *Adv. Drug Delivery Rev.*, 2022, **188**, 114449.

51 Y. Wang, W. Gao, X. Shi, J. Ding, W. Liu, H. He, K. Wang and F. Shao, *Nature*, 2017, **547**, 99–103.

52 (*a*) D. Wong, C. H. Yeo and W. H. Ang, *Angew. Chem., Int. Ed.*, 2014, **53**, 6752–6756; (*b*) J. Yu, S. Liu, Y. Wang, X. He, Q. Zhang, Y. Qi, D. Zhou, Z. Xie, X. Li and Y. Huang, *Bioact. Mater.*, 2022, **7**, 389–400; (*c*) N. Wang, Z. Wang, Z. Xu, X. Chen and G. Zhu, *Angew. Chem., Int. Ed.*, 2018, **57**, 3426–3430.

